73rd International Astronautical Congress (IAC) Paris, France, 18-22 September 2022.

IAC-22,A3,4B,7,x70326

Simulation of the detectability of different surface properties with bistatic radar observations

Jonas Krumme[1,*], Thomas P. Andert[2], René Weller[1], Graciela González Peytaví[2], Gabriel Zachmann[1], Dennis Scholl[2], Adrian Schulz[2]

[1] *Institute for Computer Graphics and Virtual Reality, University of Bremen, Bibliothekstraße 5, 28359 Bremen, Germany*

[2] *Institute of Space Technology and Space Applications, Universität der Bundeswehr München, Werner-Heisenberg-Weg 39, 85577 Neubiberg, Germany*

[*] Corresponding Author (jkrumme@uni-bremen.de)

Abstract

Bistatic radar (BSR) is a well-established technology to probe surfaces of planets and also small bodies like asteroids and comets. The radio subsystem onboard the spacecraft serves as the transmitter and the ground station on Earth as the receiver of the radio signal in the bistatic radar configuration. A part of the reflected signal is scattered towards the receiver which records both the right-hand circular polarized (RHCP) and left-hand circular polarized (LHCP) echo components. From the measurement of those, geophysical properties like surface roughness and dielectric constant can be derived. Such observations aim at extracting the radar reflectivity coefficient of the surface, which is also called the radar-cross section. This coefficient depends on the physical properties of the surface.

We developed a bistatic radar simulation tool that utilizes hardware acceleration and massively-parallel programming paradigms available on modern GPUs. It is based on the Shooting and Bouncing Rays (SBR) method (sometimes also called Ray-Launching Geometrical Optics), which we have adapted for the GPU and implemented using hardware-accelerated raytracing. This provides high-performance estimation of the scattering of electromagnetic waves from surfaces, which is highly desirable since surfaces can become very large relative to the surface features that need to be resolved by the simulation method.

Our method can, for example, deal with the asteroids 1 Ceres and 4 Vesta, which have mean diameters of around 974 km and 529 km, resp., which are very large surfaces relative to the sizes of the surface features. But even smaller objects can require a large number of rays for sampling the surface with a density large enough for accurate results.

In this paper, we present our new, very efficient simulation method, its application to several examples with various shapes and surface properties, and examine limits of the detectability of water ice on small bodies.

Keywords: Bistatic Radar, Radio Science, GPU, Shooting and Bouncing Rays

1 Introduction

One of several methods to study the properties of planetary surfaces with the help of a spacecraft is the so-called bistatic radar technique. In contrast to monostatic radar, the transmitter and receiver are spatially separated. First downlink BSR observations, in which the spacecraft acts as the transmitter and the ground station on Earth as the receiver, have been carried out on the moon [1], followed by Venus, Mars [2], Titan [3], and even on Pluto [4] and the comet 67P/Churyumov-Gerasimenko [5].

With bistatic radar, a combination of the physical structure and electrical properties of the body of interest can be studied. From these observations, information of the surface roughness, i.e., root-mean-square (RMS) slopes (ζ), near-surface dielectric constant (ϵ) and density (ρ) can be obtained. This information can be interesting for the selection of landing sites for planetary landers and rovers and also to detect water ice.

The radar equation which gives echo power from the surface includes among others the radar cross section. It can only be derived analytically for simple objects. For complex bodies, a numerical approach is needed. The software package presented in the following was developed as part of the KaNaRiA mission (cognition-based autonomous navigation using the example of resource mining in space) [6] for which the reference scenario is an "asteroid mining mission" in the main asteroid belt between Mars and Jupiter.

In the next section, an overview of the bistatic radar technique is given and the corresponding equations are provided on how to derive the dielectric properties from measurements. In section 3, our Shooting and Bouncing Rays implementation is described in detail and explains how the software was validated against test cases. Section 6 shows the different models for the shape of the central body on which we applied our Shooting and Bouncing Rays method and gives an overview of the results for the radar cross section. Section 7 summarizes and concludes the paper.

2 Bistatic Radar

The incremental echo power dP_R from a small surface element dS is given by the radar equation [7] as

$$dP_R = \frac{P_T G_T}{4\pi R_T^2} \sigma \frac{A_R}{4\pi R_R^2} dS \tag{1}$$

where

- P_T is the transmitted power,
- G_T is the transmitting antenna gain in the direction of the surface element,
- R_T is the distance from the transmitter to the surface element,
- A_R is the effective area of the receiving antenna aperture (which may, like G_T, be directional),
- R_R is the distance from the surface element to the receiver,
- and $\sigma(\phi, \varepsilon)$ the specific radar cross section (RCS).

The radar cross section σ is a measure of the efficiency in transmitting energy from the transmitter to the receiver and is defined as the ratio of the scattered field strength E_S and the incident field strength at target E_i with R as the distance between transmitter and target

$$\sigma = \lim_{R \to \infty} 4\pi R^2 \frac{|E_s|^2}{|E_i|^2} \tag{2}$$

For many quasi-specular planetary surfaces, the expression derived by Hagfors ([8], [9]) has become widely used in planetary radar surveys because it provides good agreement with measured data in many cases.

$$\sigma_0 = \frac{\phi_i C}{2} \left(\cos^4 \gamma + C \sin^2 \gamma\right)^{-\frac{3}{2}} \tag{3}$$

with

- γ the facet tilt angle at the specular point at the surface
- C a parameter interpreted as the inverse squared surface roughness in radians,
- ρ_i are the Fresnel reflection coefficients for the different polarization's.

$$R_H = \frac{\cos\phi - \sqrt{\varepsilon - \sin^2\phi}}{\cos\phi + \sqrt{\varepsilon - \sin^2\phi}} \tag{4}$$

$$R_V = \frac{\varepsilon\cos\phi - \sqrt{\varepsilon - \sin^2\phi}}{\varepsilon\cos\phi + \sqrt{\varepsilon - \sin^2\phi}} \tag{5}$$

with ϕ the incident angle at the specular point and ε the dielectric constant. The same (SC) and opposite (OC) sense of circular polarization can be expressed as

$$R_{SC} = \frac{R_V + R_H}{2} \tag{6}$$

$$R_{OC} = \frac{R_V - R_H}{2} \tag{7}$$

i.e. if RHCP is the transmitted circular polarization then R_{SC} gives the amplitude of the reflected wave and R_{OC} the LHCP echo amplitude. For more information see for example [10], [2], [7].

Only for simple objects like a sphere the radar cross section σ can be derived in an analytical way. For more complex objects the RCS can only be derived numerically. One method which can be applied to derive the RCS numerically is described in the next section.

3 Shooting and Bouncing Rays

3.1 Implementation

The Shooting and Bouncing Rays (SBR) method described in this paper is based on [11], with the generalization of [12] to arbitrary objects. The SBR method represents an incident plane wave by a dense grid of rays (see Figure 1). The electromagnetic wave is assumed to be planar near the target for which the scattering is to be computed.

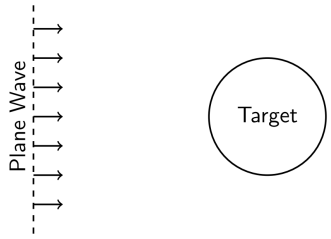

Figure 1: Plane wave approaching a target.

As the electromagnetic wave is planar we can represent it as a rectangle so that the plane wave can easily be expressed by a grid of rectangular ray tubes, where each ray tube covers a small area of the plane wave. This ray tube grid should be large enough so that the plane wave covers all relevant parts of the target that are visible from the direction of the incoming plane wave. Every ray tube represents a small part of the electromagnetic wave, which can be individually calculated and traced into the scene with the target object. The SBR method is divided into three main parts according to [11]:

1. Ray tracing,
2. Amplitude tracking, and

3. Physical optics.

In the first part, rays are sent into the scene and the hit points of the ray with the target are recorded. The second step calculates the electromagnetic field of each ray while it bounces/reflects from the objects in the environment until no more intersection points can be found. The last part calculates the scattered field in the direction of the observation; it is based on the approximations of physical optics. After calculating the contribution of each ray, we can accumulate the individual contributions to estimate the scattering of the electromagnetic wave from the target. In the following, the three parts are described in more detail.

3.2 Step 1. Ray Tracing

For the first step, we find the intersection points of the ray with the surface of a target object and calculate reflected rays until no more intersection points with the surface can be found. The origins of the initial rays which are used for representing the plane wave lie inside the rectangle which makes up the incident plane wave and the initial direction of those rays equals the propagation direction of the electromagnetic wave at that point. Because the wave is assumed to be plane here they all have the same initial direction. The reflected rays are calculated such that they satisfy the following rules:

1. The reflected ray lies in the plane of incidence

2. The angle of reflection equals the angle of incidence

The plane of incidence (figure 2) is the plane that contains the direction vector of the incoming ray and the normal vector of the surface at the intersection point.

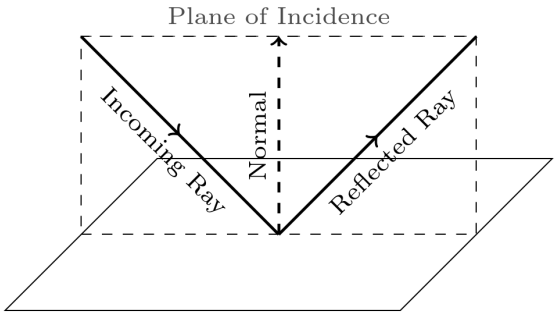

Figure 2: Plane of Incidence

When the surface normal $\mathbf{n}$ and the direction of the incoming ray $\mathbf{d}_i$ is given we can calculate the direction of the reflected ray $\mathbf{d}_r$ using the following equation:

$$\mathbf{d}_r = \mathbf{d}_i - 2(\mathbf{d}_i \cdot \mathbf{n})\mathbf{n} \tag{8}$$

The reflected ray can be constructed by setting the origin of the ray to the intersection point between the incoming ray and the surface and setting the direction to $\mathbf{d}_r$. This can be repeated until no more intersection point for the reflected ray can be found or the number of intersection points of a ray exceeds some previously set threshold.

3.3 Step 2. Amplitude Tracking

The second part of the SBR method uses the calculated intersection points of each ray to determine the electromagnetic field of each ray tube at the exit aperture using geometrical optics. There are different choices for the exit aperture[13] which is used in the last part of the SBR method to determine the final field which is scattered into the observation direction by using physical optics. Here the object itself is used as the exit aperture as proposed by [12]. This way we only need to trace the rays until no more intersection points can be found and no intersection with a special exit aperture surface/object must be determined. In [11] two different types of rays for calculating the electromagnetic field are used. The two types of rays have different objectives and are **1.** corner rays and **2.** central rays. The corner rays of each ray tube are used to calculate the shape and the size of the electromagnetic wave represented by the ray tube at the exit aperture and the central rays are used to actually track the electromagnetic field of the ray tube from the plane wave to the exit aperture. With this approach, each ray tube consists of 5 rays. However neighboring ray tubes can share corner rays. Sharing the corner rays reduces the total number of rays that need to be calculated. Figure 3 shows a single ray tube which consists of the four corner rays $\mathbf{c}_0$, $\mathbf{c}_1$,$\mathbf{c}_2$,$\mathbf{c}_3$ and a single central ray $\mathbf{r}$.

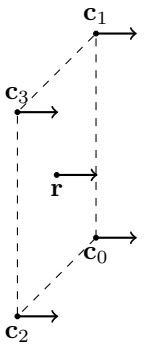

Figure 3: Single Ray Tube

The only relevant information for the corner rays is the intersection point at the exit aperture. Because of this, we can trace the corner rays as shown previously in step 1 and just store the last intersection point. However, the central ray must track the electromagnetic field from the initial starting point inside the plane wave to the last intersection point at the exit aperture. This means that there is some more work to be done for each intersection point. Given the intersection points which are calculated in the previous step, we can calculate the electromagnetic field at the exit aperture using geometrical optics. The incident plane wave (similar to the formulation by [11]) is given by

$$\mathbf{E} = [\hat{\theta}I + \hat{\phi}\bar{I}]e^{\mathbf{k}^i \cdot \mathbf{r}} \tag{9}$$

where I is the amplitude of the vertical polarization, $\bar{I}$ is the amplitude of the horizontal polarization, $\mathbf{k}^i$ is the observation direction and $\mathbf{r}$ is some point in space. $\hat{\phi}$ and $\hat{\theta}$ are the spherical unit vectors[13] and can be calculated from the observation direction (r, θ, ϕ). Based on the incoming electromagnetic field at some intersection point we can calculate the reflected electromagnetic field by geometrical optics using the following equation for each intersection point[11]:

$$\mathbf{E}_r = (DF)_i \cdot \Gamma_i \cdot \mathbf{E}_i \cdot e^{-j(phase)} \tag{10}$$

Here $\mathbf{E}_r$ represents the reflected field at the intersection point, DF_i is the divergence factor which represents the spreading of the ray tube while traveling through space, Γ_i represents the reflection coefficients of the material at the intersection point, $\mathbf{E}_i$ represents the incoming electromagnetic field at the intersection point and the last term incorporates the phase of the electromagnetic wave. A detailed description of the divergence factor is given by Ling et. al[11]. However for triangle based meshes this factor can be ignored because in general the divergence factor is restricted to an analytic representation of surfaces where the information of the curvature at the intersection point is available[14]. Because the focus here is on triangle meshes we ignore the divergence factor when calculating the reflected field. The $(phase)$ part of the last term is just the distance between the origin of the incoming ray and current intersection point and can be calculated for the origin $\mathbf{o}$ and the reflection point $\mathbf{r}_i$ as

$$(phase) = ||\mathbf{o} - \mathbf{r}_i|| \tag{11}$$

To apply the reflection coefficients Γ_i we need to decompose the incident field $\mathbf{E}_i$ into its TE (transverse electric) and TM (transverse magnetic) components[11]. Following [15] the reflected field at each intersection point can be calculated from the incident field $\mathbf{E}_i$ and the reflection coefficients $\Gamma_{||}$ and $\Gamma_{\perp}$ as follows:

$$\begin{bmatrix} E^r_{||} \\ E^r_{\perp} \end{bmatrix} = \begin{bmatrix} \Gamma_{||} & 0 \\ 0 & \Gamma_{\perp} \end{bmatrix} \begin{bmatrix} E^i_{||} \\ E^i_{\perp} \end{bmatrix} \tag{12}$$

The matrix consisting of $\Gamma_{||}$ and $\Gamma_{\perp}$ represents the Γ_i term. The incident field can be decomposed into its TE and TM components using the following equations:

$$E^i_{||} = \hat{\mathbf{e}}_{||} \cdot \mathbf{E}_i \tag{13}$$

$$E^i_{\perp} = \hat{\mathbf{e}}_{\perp} \cdot \mathbf{E}_i \tag{14}$$

Let $\hat{\mathbf{k}}^i$ be the propagation direction of the electromagnetic field (the propagation direction of the geometrical optics ray) before the intersection, $\hat{\mathbf{k}}^r$ the propagation direction after the intersection and $\hat{\mathbf{n}}$ be the normal of the surface at the intersection point. Than $\hat{\mathbf{e}}_{||}$ and $\hat{\mathbf{e}}_{\perp}$ can be calculated as follows:

$$\hat{\mathbf{e}}_{||} = \frac{\hat{\mathbf{k}}^i \times \hat{\mathbf{e}}_{\perp}}{||\hat{\mathbf{k}}^i \times \hat{\mathbf{e}}_{\perp}||} \tag{15}$$

$$\hat{\mathbf{e}}_{\perp} = \frac{\hat{\mathbf{k}}^i \times \hat{\mathbf{n}}}{||\hat{\mathbf{k}}^i \times \hat{\mathbf{n}}||} \tag{16}$$

After calculating the decomposed electromagnetic field for the reflected ray we need to reconstruct the electromagnetic field from the decomposed parts. This can be done using the following equation:

$$\mathbf{E}_r = \hat{\mathbf{e}}^r_{||} \cdot E^r_{||} + \hat{\mathbf{e}}_{\perp} \cdot E^r_{\perp} \tag{17}$$

The vector $\hat{\mathbf{e}}^r_{||}$ can be calculated from $\hat{\mathbf{e}}_{\perp}$ as:

$$\hat{\mathbf{e}}^r_{||} = \frac{\hat{\mathbf{k}}^r \times \hat{\mathbf{e}}_{\perp}}{||\hat{\mathbf{k}}^r \times \hat{\mathbf{e}}_{\perp}||} \tag{18}$$

$\Gamma_{||}$ and $\Gamma_{\perp}$ are the reflection coefficients of the surface at the intersection point. For perfectly electric conducting objects, they can be set to -1 [16]. There are different ways to calculate the reflection coefficients for the given surface depending on the material or other properties like roughness. One way is to use the fresnel reflection coefficients[17]

3.4 Step 3. Physical Optics

The third and last step is used to calculated the contribution of each triangle-based on the Physical Optics approach. Using the electromagnetic field calculated at the exit aperture using geometrical optics we can now calculate the contribution of this ray tube given an observation point (r, θ, ϕ). At such an observation point in the far field the contribution of the ray tube can be expressed as[12]

$$\mathbf{E}(r, \theta, \phi) \approx \frac{e^{-jkr}}{r}(\hat{\theta}A_{\theta} + \hat{\phi}A_{\phi}) \tag{19}$$

where A_{θ} and A_{ϕ} can be calculated by

$$\begin{bmatrix} A_{\theta} \\ A_{\phi} \end{bmatrix} = \left(\frac{jk}{2\pi}\right) \iint_{\text{tube}} e^{j\mathbf{k}\cdot\mathbf{r}} \left\{ \begin{bmatrix} -\hat{\phi} \\ \hat{\theta} \end{bmatrix} \times \mathbf{E}_{ap}(\mathbf{r}) f_e + Z_0 \begin{bmatrix} \hat{\theta} \\ \hat{\phi} \end{bmatrix} \times \mathbf{H}_{ap}(\mathbf{r}) f_h \right\} \cdot \hat{\mathbf{n}} dxdy \tag{20}$$

with $\mathbf{E}_{ap}(\mathbf{r})$ and $\mathbf{H}_{ap}(\mathbf{r})$ representing the electric and magnetic field of a ray tube at the exit aperture for point $\mathbf{r}$ (the last intersection point calculated with geometrical optics). $\mathbf{k}$ represents the wave vector of the electromagnetic wave and can be calculated by

$$\mathbf{k} = k((\cos(\phi^i)\hat{\mathbf{x}} + \sin(\phi^i)\hat{\mathbf{y}})\sin(\theta^i) + \cos(\theta^i)\hat{\mathbf{z}}) \quad (21)$$

Assuming that the ray tubes are small enough the following approximation can be used:

$$\begin{bmatrix} A_\theta \\ A_\phi \end{bmatrix} \approx \begin{bmatrix} B_\theta \\ B_\phi \end{bmatrix} \frac{jk}{2\pi} (\triangle A)_{\text{exit}} e^{j\mathbf{k}\cdot\mathbf{r}} P(\theta, \phi) \quad (22)$$

A detailed description of the physical optics approach and how to calculate B_θ and B_ϕ can be found in the Physical Optics section in [18]. The description there is based on [12].

4 Implementation

The previous part discussed the fundamentals necessary to implement the SBR method. Especially how to calculate the electromagnetic field based on geometric optics and physical optics for a given ray. The following section will describe and discuss the implementation details and decisions that we made for implementing the different versions of the SBR method. This also includes the ray model that we chose to implement the ray tracing part of the SBR method.

4.1 GPU Implementation

The core part of our CUDA implementation is given in Algorithm 1. The plane wave is split into a number of smaller rectangular tiles, because the targets can be very large. The size of a tile can be adjusted so that either more but smaller tiles, or fewer but larger tiles are created. Our current implementation uses a maximum tile size of 2048×2048 for both the GPU and the CPU versions. However, in CUDA we also use thread blocks with a size of 16×16 threads. This means that if a tile is smaller than 2048 rays in some direction, then the CUDA implementation uses padding so that the tile fits exactly into the thread blocks.

First, the program loops over all observations. Each observation represents a pair of directions, one for the incoming plane wave, and one for the outgoing one (in the direction of the receiver). The observation also stores the direction of the electric field for the horizontal and vertical polarization, which is used to initialize the electric field for each ray at the plane wave. In order to calculate the actual RCS, we iterate over all tiles of the plane

```
foreach observation do
    setup observation
    foreach tile in R do
        foreach tile in U do
            calculate ray contributions on the GPU
            sum ray contribution
        end
    end
    calculate RCS from ray contributions
end
```

Algorithm 1: Main loop of the implementation of our algorithm in CUDA on the GPU.

wave and calculate the rays of this tile on the GPU; we also accumulate the results of the tile on the GPU. The directions R and U are two directions orthogonal to the propagation direction of the wave and are used to specify the orientation of the rectangular plane.

4.1.1 CUDA

Our CUDA implementation covers the ray tracing part of the SBR method. We use a bounding volume hierarchy (BVH) in order to speed up the ray-geometry intersection calculations. This, and the ensuing ray-triangle intersection are implemented directly inside a CUDA kernel. The BVH is constructed on the CPU and then copied to GPU memory using a compact representation based on a linear array of nodes. The algorithm for building such a BVH, the traversal algorithm, and the layout to store it on the GPU can be found in [19]. A CUDA kernel is launched for each tile and a thread for each ray. Each ray's contribution to the RCS of the target object is stored in global memory. To accumulate all contributions of all rays we use a reduction operation provided in the thrust library [20].

4.2 Discrete Rays vs. Ray Tubes

One decision that needs to be made is to choose between discrete rays or ray tubes. For example, [21] successfully used discrete rays instead of ray tubes consisting of four corner rays. One advantage of discrete rays is that it reduces the number of rays that need to be traced when calculating the RCS of a given object. It also reduces the need for synchronization when calculating the RCS on the Graphics Processing Unit (GPU). For instance, when each thread calculates the path of a single ray, we would need to wait for all corner rays plus the central ray to finish before the final aperture integration can be done for the electromagnetic field. It is possible to calculate all rays in a single thread, but this would drastically increase the work which needs to be done as the corner rays of neighboring ray tubes aren't shared anymore between the ray tubes. So the same corner ray would need

to be calculated multiple times in different threads. This would further increase the time needed to trace all necessary rays. Another reason for discrete rays instead of ray tubes is that when using ray tubes we have to deal with potentially highly divergent ray tubes. This could happen, for example, when two corner rays hit different triangles with very different normal vectors. This could lead to four corner rays where the last intersection points are at vastly different positions on the target object. In such cases it could be problematic to use such corner rays to represent the shape of the ray tube (e.g. the shape represented by the corner rays might not coincide with the surface of the target object).

Also, this could lead to corner rays which wouldn't necessarily lie in a common plane when we use four corner rays for a ray tube. In the case of a triangle-based representation, this could only be guaranteed if the last intersection point of all corner rays is inside the same triangle. Using a triangular ray tube we could always create a plane where all three corner rays lie inside a common plane. However, there is still the problem of a highly divergent ray tube. One solution was proposed by [15] where they only accept ray tubes for calculating the physical optics approximation at the exit aperture when all corner rays hit the same triangle. This also ensures that each point inside the ray tube lies in a common plane. However, this approach would exclude some parts of the target shape from the RCS calculation because ray tubes at the edges between two triangles would be ignored. In the case of a mesh with a high density of triangles, a lot of ray tubes would be ignored. Therefore, a discrete ray approach was finally chosen.

5 Verification

We tested our SBR implementation with a set of different objects: a sphere, a cylinder, a dihedral corner reflector, and two different versions of trihedral corner reflectors. The first two objects are represented by a function that directly allows for the calculation of the intersection point with a geometrical optics ray. Here the results for the dihedral corner reflector are reported.

The material of the test objects is assumed to be a perfect electrical conductor which should have reflection coefficients of -1 for both polarization cases as noted previously [22]. However, the tests revealed that these values don't seem to apply to the implementations of the geometrical optics calculation used here based on the approach presented by [15]. Comparing the results with the reflection calculations based on [23] for this special case of total reflection seems to indicate that the values -1 and 1 need to be used. This might be due to the way the reflected vectors are calculated by [15]. Overall these values lead to correct results for multiple reflections and reflection directions which are more in line with the reflection calculations presented by [23]. But this should be taken into account when extending the process to dielectric materials.

For the test, we use a dihedral corner reflector with a side length of 1m for both plates. The frequency for the RCS calculations is 1GHz and the observation is done for a fixed $\theta = 90^\circ$ and for ϕ from 0° to 90°. Again the observation points lie in the xy-plane. The increment is 1° which again leads to 90 observation points. Here we report the results for both HH-polarization(horizontal to horizontal) and VV-polarization(vertical to vertical). Figure 5 shows the result for the observation points at 1GHz for HH-polarization.

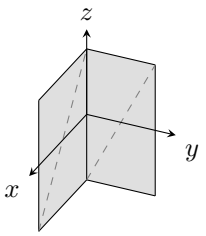

Figure 4: Dihedral Corner Reflector

Results for both settings were reported by [23]. Here we compare both results from 0° to 45° with the reported results because the results are mirrored at $\phi = 45^\circ$. When comparing the results we can see that overall they agree very well at most points. However, they report a minimum RCS for the HH-polarization of around 3dbsm while the implementation shown here has a minimum RCS which goes further down to around 0 for the HH-polarization case. Also, the first local maximum after the minimum is reported to be around 15-16 while it only goes up to 13-14 for the current implementation. However, the next local maximum at around 20° agrees well with the results reported by [23]. Also the global maximum at $\phi = 45^\circ$ near 25dbsm agrees well with the reported results by [23]. Overall the HH-polarization case shows some deviations around 10° and 80° where the minimum RCS is reached. The reported RCS here is smaller than would be expected from the results reported by [23]. A similar effect can be seen for the VV-polarization case but reversed. The reported results have a minimum RCS of 10dbsm around 10° and 80° while the results from this implementation have a minimum of around 13dbsm at these observation angles.

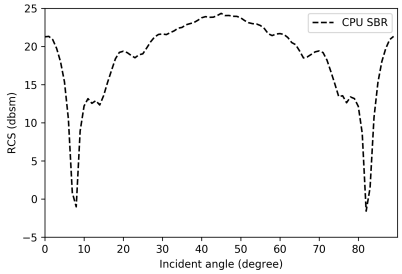

Figure 5: HH-polarization result for $\theta = 90°$ at 1GHz

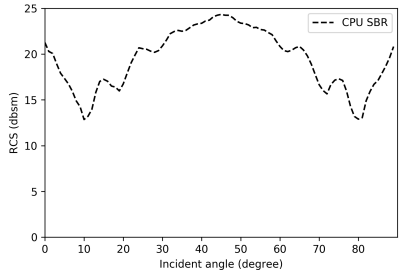

Figure 6: VV-polarization result for $\theta = 90°$ at 1GHz

However, the following local maximum at around $15°$ of $\approx$ 17dbsm agrees well with the reported results by [23]. Overall we can see that the implementation seems to have some deviations at the first minimum point for both polarization cases. The implementation shown here reports lower values for the first minimum when calculating the HH-polarization and higher values for the VV-polarization case. However, the results after this first minimum agree very well with the results reported by [23]. The reason for this deviation might be that we use a discrete ray that doesn't track the shape of the ray tube at the exit aperture very well. When the observation point is at $\phi \approx 10°$ some rays reflect from the plate in the yz-plane onto the plate in the xz-plane and reflect from this plate back to the receiver. However, the angle at the second reflection between the surface normal and the ray direction should be relatively high and around $80°$. It seems that for such cases there is some deviation between the reported results and the calculated RCS using our approach. The reported results for $\phi = 45°$ again agree very well with the reported results from [23].

6 Results

The following scenario is defined to be representative of a small body mission with the following parameters: Transmitter and receiver are placed in a circular orbit of about 1 km from the surface of the central body for simplicity. In the monostatic case, the transmitter and receiver are at the same location. In the bistatic case, the location of the transmitter and receiver is separated by the incidence angle ϕ. The dielectric constant ε on the surface is handed over as color coding in the shape model to the software package. In order to reduce complexity, the dimensions of the scenario have been scaled down by a factor of 25. The next section shows the results for a spherical shape of the central body.

6.1 Sphere

A spherical shape of the central body with a radius of 50 m (see figure 7) with a constant dielectric constant ε = 3 and with variations of the dielectric constant ε (see figure 10) is assumed.

6.1.1 Monostatic case sphere

In the monostatic configuration, the transmitter and receiver are located at the same position, i.e. the selected circular orbit of both are identical. Due to the symmetric geometry and if a constant dielectric constant ε is used for the entire surface of the sphere the RCS shall be constant over the orbit. For the simulation a dielectric constant ε = 3 is assumed and in figure 8 both the radar cross section of the same RCS_{SC} and opposite RCS_{OC} sense of circular polarization is shown. As expected the RCS_{SC} is constant over the entire track and the RCS_{OC} vanishes in the monostatic case, i.e. the incident angle ϕ = 0°.

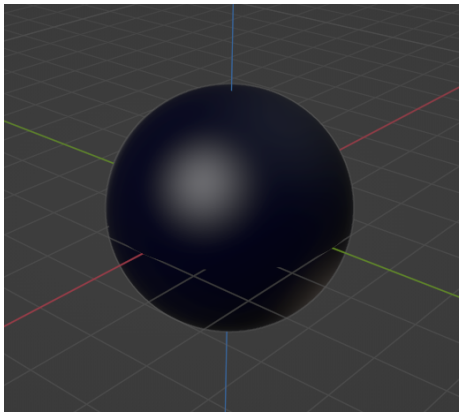

Figure 7: The central body is represented by a sphere with a diameter of 50 m and a dielectric constant ε = 3.

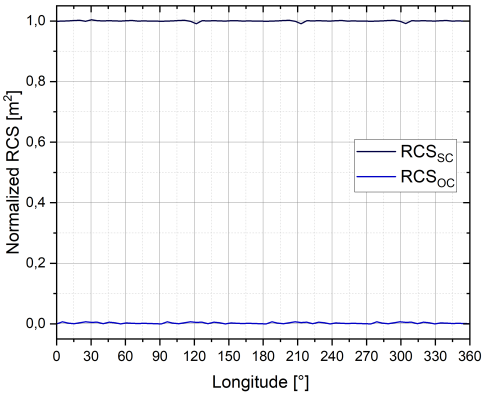

Figure 8: RCS of a sphere with a diameter of 50 m and dielectric constant ε = 3 in the monostatic case

In figure 10 the same configuration can be seen but with a sphere where each hemisphere has a different ε of 2 and 4, respectively. The resulting RCS decreases with lower ε in the center between around 45° and 135° as it can be seen in figure 9. The RCS_{OC} vanishes as expected but shows also very small numerical noise and the transfer regions between the two different hemispheres.

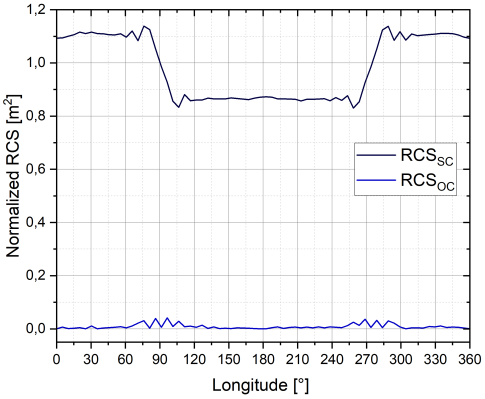

Figure 9: RCS of a sphere with a radius of 50 m and dielectric constant ε = 2,4 in the monostatic case

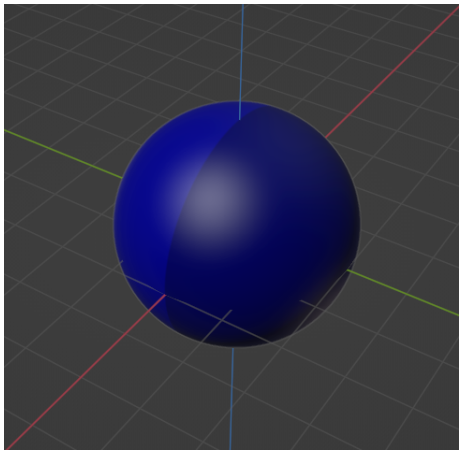

Figure 10: The central body is represented by a sphere with a radius of 50 m. The sphere is subdivided into two parts with a dielectric constant ε = 2, 4

6.1.2 Bistatic case sphere

In the bistatic case, the position of the transmitter and receiver are separated by the incident angle ϕ. An incident angle larger than 0° (monostatic case) results in an increasing radar cross section of the opposite polarisation RCS_{OC} as it can found in figure 11, where it is shown for $\phi = 65°$ and a constant ε = 3.

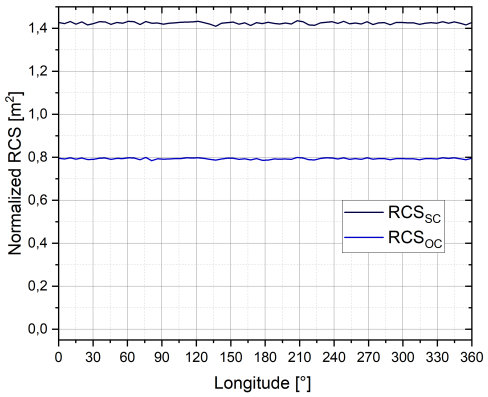

Figure 11: RCS of a sphere with dielectric constant ε = 3 in the bistatic case incident angle $\phi = 65°$

The same is true if the dielectric constant is changing on the surface of the sphere as in figure 10 where to each hemisphere a different ε of 2 and 4 is assigned. A smaller ε increases the RCS of the opposite polarization RCS_{OC} and decreases the RCS of the same polarization RCS_{SC} (see figure 12).

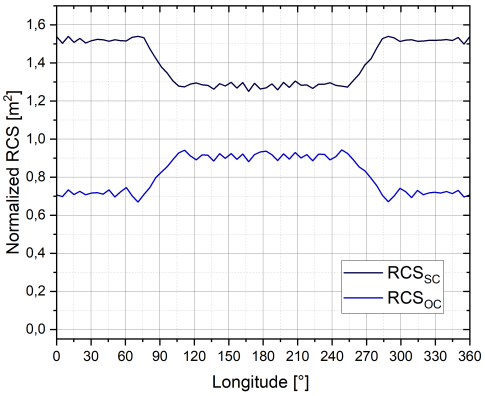

Figure 12: RCS of a sphere with dielectric constant ε = 2,4 in the bistatic case at incident angle $\phi = 65°$

6.2 *Ellipsoid*

Here, the spherical central body is replaced with an ellipsoid ($50 \times 44 \times 35$ m), but the circular orbit of the transmitter and receiver is kept the same as in the section before.

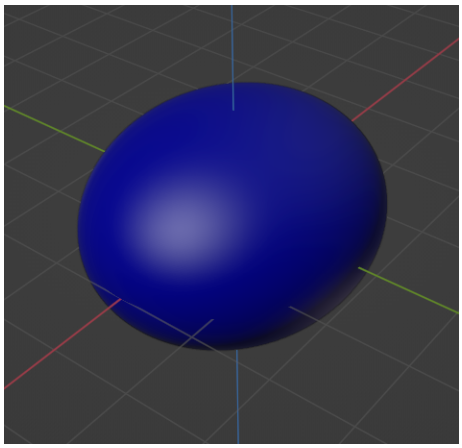

Figure 13: The central body is represented by an ellipsoid with the semi-major axis $50 \times 44 \times 35$ m. The ellipsoid has a dielectric constant ε = 3.

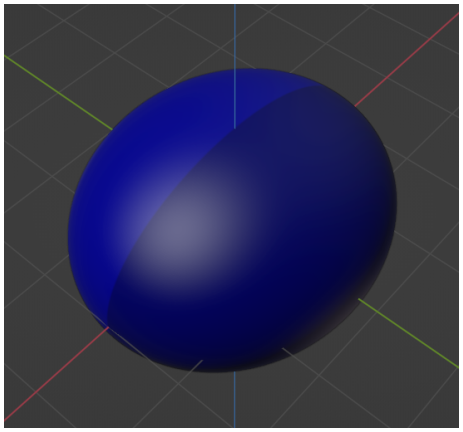

Figure 14: The central body is represented by an ellipsoid with the semi-major axis $50 \times 44 \times 35$ m. The ellipsoid is subdivided into two parts with a dielectric constant ε = 2, 4.

6.2.1 *Monostatic case ellipsoid*

Here, the circular orbit of the transmitter and receiver are again identical. The distance to the surface is changing because of the ellipsoidal shape of the central body (see figure 13) and the circular orbit. For the simulation, a dielectric constant ε = 3 is used (see figure 15). Due to the changing geometry, the radar cross section is no longer constant and is changing with the varying distance to the surface of the ellipsoid. The resulting curve of theRCS of the same polarization RCS_{SC} shows a sinusoidal behavior. The two peaks correspond to the closest approach distance between the transmitter/receiver and the surface of the ellipsoid.

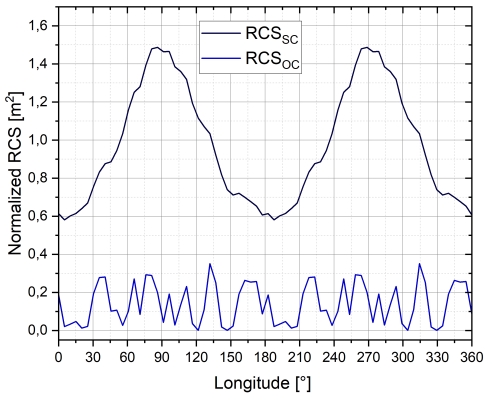

Figure 15: RCS of an ellipsoid ($50 \times 44 \times 35$ m) with dielectric constant ε = 3 in the monostatic case

If the dielectric constant ε varies as is the case and also the distance to the central body varies the resulting RCS

of the same polarization RCS_{SC} shows again a sinusoidal shape but the two peaks no longer have the same amplitude (figure 16). This is because with a lower ε also the RCS decreases.

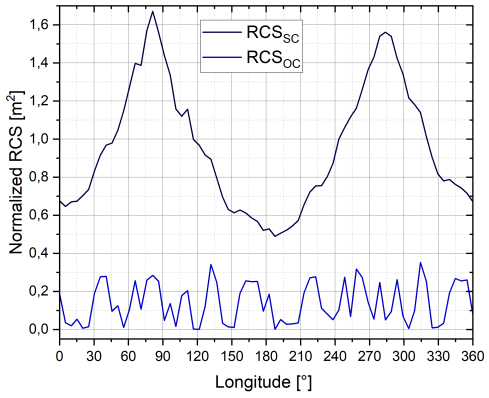

Figure 16: RCS of an ellipsoid ($50 \times 44 \times 35$ m) with dielectric constant ε = 2,4 in the monostatic case

6.2.2 *Bistatic case ellipsoid*

As is normal in the bistatic case, the position of the transmitter and receiver are separated by the incident angle ϕ. An incident angle larger than 0° (monostatic case) results in an increasing radar cross section of the opposite polarisation RCS_{OC} as it can be seen in figure 17, where is shown for $\phi = 65°$ and a constant ε = 3. Both, RCS_{OC} and RCS_{SC}, show a sinusoidal shape that is caused by the changing distance between transmitter/receiver and surface but with different amplitudes.

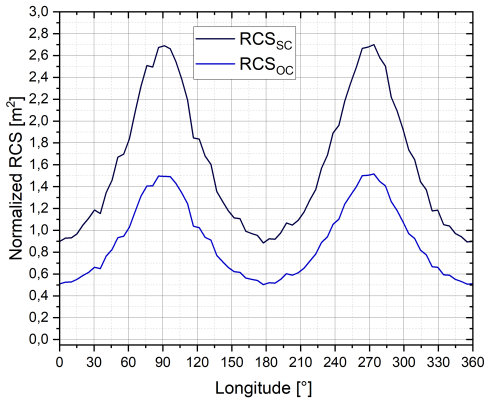

Figure 17: RCS of an ellipsoid with dielectric constant ε = 3 in the bistatic case incident angle $\phi = 65°$

If the dielectric constant is changing on the surface, each hemisphere has a different ε of 2 and 4 (figure 10), both RCS_{OC} and RCS_{SC}, having again a sinusoidal curvature, but due to the difference in ε the amplitude of the peaks are differing as shown in figure 18. In contrast to the monostatic case the difference in the amplitude of the peaks in each polarization is smaller in the bistatic case.

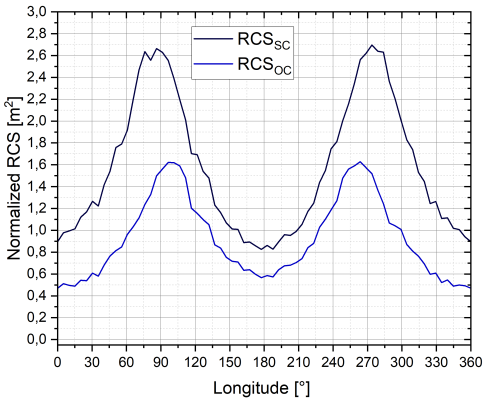

Figure 18: RCS of an ellipsoid with dielectric constant ε = 2,4 in the bistatic case at incident angle $\phi = 65°$

6.3 *Ellipsoid with crater*

In order to see the effect of topographic features in the radar cross section the central body is again an ellipsoid ($50 \times 44 \times 35$ m), but with a crater on the surface with a diameter of 12.5 m and depth of 22.5 m (figure 19). The crater is located in the $x-y$ plane at around 45 longitude. The circular orbit of the transmitter and receiver is the same as in the simulations before.

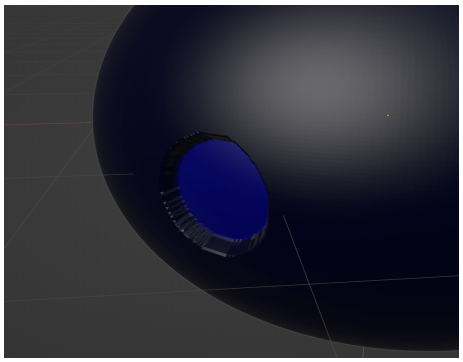

Figure 19: The central body is represented by an ellipsoid with the semi-major axis ($50 \times 44 \times 35$ m). The ellipsoid has a crater with a diameter of 12.5 m and a depth of 22.5 m. The area inside the crater is assigned with different values for the dielectric constant ε

6.3.1 *Monostatic case ellipsoid with crater*

The comparison of the RCS for an ellipsoid alone (figure 15) and an ellipsoid with crater (figure 20) shows that the overall shape is similar in the monostatic case, but a small peak at 45 of the RCS in figure 20 shows the influence of the small crater on the radar cross section of the same polarization RCS_{SC}. But it can also be observed that the numerical noise increased for both the same and opposite polarization.

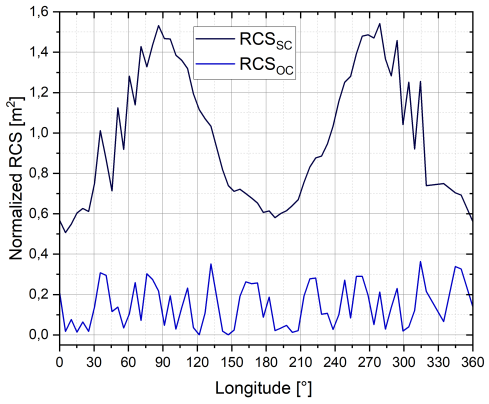

Figure 20: RCS of an ellipsoid with crater and an overall dielectric constant ε = 3 in the monostatic case.

If the crater bottom is assigned with a dielectric constant $\varepsilon = 3.2$ (water ice) which is different to the surrounding surface with $\varepsilon = 3$ (rock) the impact of the different dielectric constant disappears in the noise as it is shown in figure 21. The shape of the RCS is clearly dominated by the shape and distance variation.

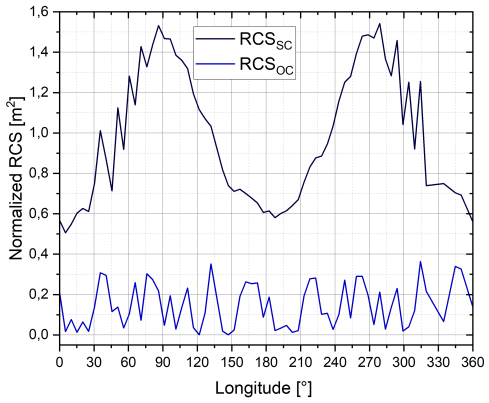

Figure 21: RCS of an ellipsoid with a crater and dielectric constant ε = 3.2 in the crater and ε = 3 outside in the monostatic case

6.3.2 *Bistatic case ellipsoid with crater*

In the bistatic case, the opposite polarisation RCS_{OC} becomes more prominent with increasing incident angle ϕ. This also means that surface features like a crater have an impact on both the opposite polarization RCS_{OC} and the same polarization RCS_{SC} radar cross section, respectively. In figure 22 no impact at 45 can be observed in compared to the crater-free ellipsoid in figure 17 but again and increase of numerical noise in the RCS can be observed.

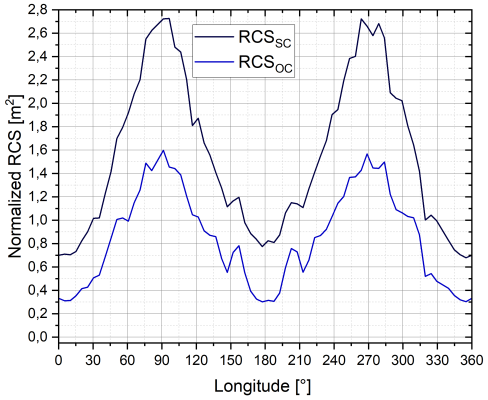

Figure 22: RCS of an ellipsoid with a crater on the surface and an overall dielectric constant ε = 3 in the bistatic case incident angle $\phi = 65°$

Taking into account in the bistatic case a difference between the crater bottom ($\varepsilon = 3.2$) and the outside surface ($\varepsilon = 3$) both RCS_{SC} and RCS_{OC} (see figure 23) should deviate from the case in which the same dielectric constant ε for the entire surface was used (see figure 17). Since $\Delta\varepsilon$ is small also the difference in RCS seems to disappear in the numerical noise, i.e. the overall shape is dominated by the variation in distance and by the incident angle ϕ.

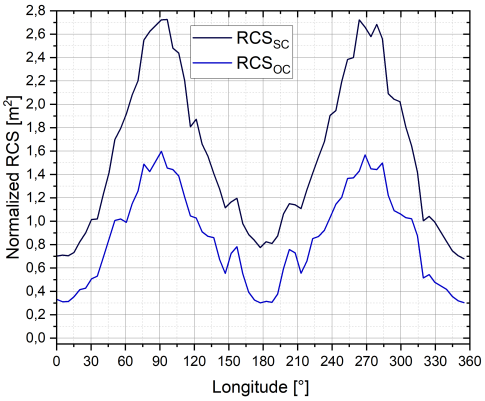

Figure 23: RCS of an ellipsoid with a crater on the surface and a dielectric constant ε = 3.2 in the crater and ε = 3 outside in the bistatic case at an incident angle $\phi = 65°$

6.4 Performance

We tested the performance of our CUDA implementation of the Shooting and Bouncing Rays algorithm against a OptiX implementation currently in development that makes use of RT Cores by applying it to a body with a complex structure; here, we chose the asteroid Vesta (see Figure 24). The shape model we used is from [24] and consists of 256 000 triangles. The original size of Vesta [25] provided by the shape model was scaled down to the dimensions 576m $\times$ 556m $\times$ 467m, so that the observation points can be calculated in a reasonable time.

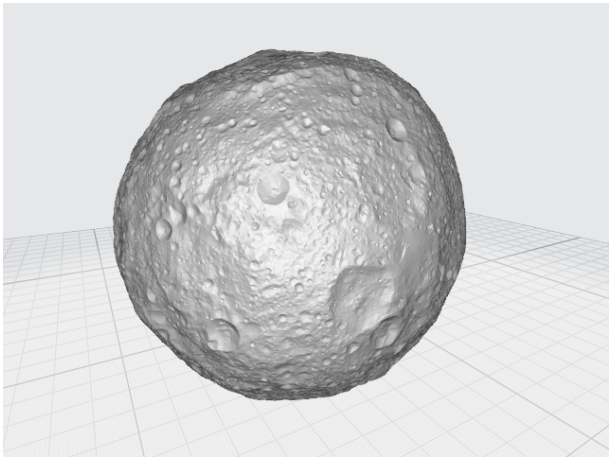

Figure 24: Shape model of Vesta taken from [24].

The test is performed with an RTX 2080 Super GPU from NVIDIA with 48 RT Cores and takes into account 90 observation points for ϕ from 0° to 90° and a fixed $\theta = 90°$ using a frequency of 5GHz. For the Vesta model, we can see that the OptiX implementation which can leverage hardware-accelerated ray tracing, is approximately twice as fast when comparing it to the current CUDA implementation. The OptiX implementation also seems to be less effected when different parts of the object are observed. The CUDA implementation shows some visible differences regarding the run-time for some incidence angles as shown in Figure 25. The observations between $\phi = 10°$ and $\phi = 60°$ need a bit more time than the observations after $\phi = 80°$. This doesn't seem to effect the OptiX implementation to the same degree. Taking a close look at the run-time of the OptiX implementation allows us to see some small differences but they don't seem to have a comparable magnitude in comparison to the CUDA version. Overall the results seem to indicate that the OptiX implementation has better performance characteristics when comparing it to the CUDA implementation. Here the OptiX version can be considered a higher-performance implementation.

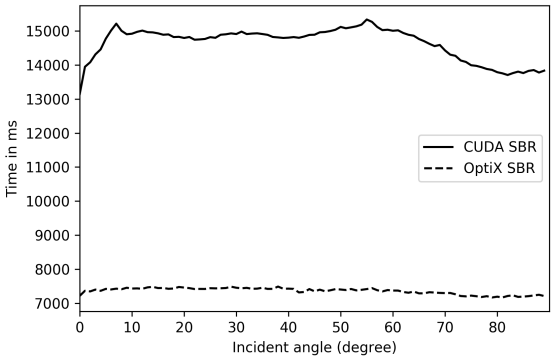

Figure 25: Performance of the CUDA implementationan of our Shooting and Bouncing Rays algorithm for Vesta.

7 Conclusions and discussions

The paper presents a very fast and efficient implementation of SBR method on the GPU, in order to better constrain the RCS of small bodies like asteroids and comets. First preliminary results are obtained by the simulation of a transmitter and receiver orbiting a central body with spherical and ellipsoidal shapes and computing from this configuration the radar cross section of the body. Also, a small crater is added to the ellipsoidal shape with different dielectric constants.

Consequently, the shape of the radar cross section curve is dominated by the varying distance between the transmitter/receiver and the surface of the central body when comparing the RCS of a sphere with an ellipsoid, assuming a circular orbit for the transmitter and receiver. Also, the incident angle ϕ influences the amplitude of the same polarization RCS_{SC} and the opposite polarization RCS_{OC}. Small topographic features like a crater or a changing dielectric constant ε therefore also appear in

both polarizations, if $\phi \neq 0$, but as a minor contribution. Therefore, in order to detect these small changes in the radar cross section for example caused by water ice in a small crater, the larger contributions need to be modeled and subtracted to detect these small contributions. With the simulation tool described here, which utilizes hardware acceleration available on modern GPUs, this contribution can be modeled. However the current calculations indicate that there might be some noise in the calculated RCS results. Currently work is done to investigate how such noise in the implementation can be reduced. For example different distributions (e.g. using Poisson sampling) of rays on the rectangular representation of the plane wave instead of the regular grid are to be considered. This could potentially reduce unwanted interactions that might arise between the triangle-based mesh used to represent the target and the regular-grid based distribution of the rays on the plane wave. Additionally switching from the current CUDA implementation to the OptiX version should also allow for faster RCS predictions.

Abbreviations

BSR bistatic radar

BVH bounding volume hierarchy

GPU Graphics Processing Unit

LHCP left-hand circular polarized

RCS radar cross section

RHCP right-hand circular polarized

SBR Shooting and Bouncing Rays

BVH bounding volume hierarchy

8 Acknowledgement

The work on the part of the University of Bremen presented in this paper was partially funded by DLR under grant 50NA1916. The work by Bundeswehr University was carried out in the frame of project KaNaRiA-NaKoRa, financed by the German Ministry of Economy and Energy and administered by the German Aerospace Center, Space Administration (DLR, Deutsches Zentrum für Luft- und Raumfahrt, FKZ 50NA1915).

References

[1] G. L. Tyler and R. A. Simpson. “Bistatic radar measurements of topographic variations in lunar surface slopes with Explorer 35.” In: *Radio Science* 5 (Feb. 1970), pp. 263–271. DOI: 10.1029/RS005i002p00263.

[2] R A Simpson et al. “Polarization in Bistatic Radar Probing of Planetary Surfaces: Application to Mars Express Data”. In: *Proceedings of the IEEE* 99.5 (May 2011), pp. 858–874. ISSN: 0018-9219, 1558-2256. DOI: 10.1109/JPROC.2011.2106190.

[3] M. Pérez-Ayúcar et al. “Bistatic observations of Titan’s surface with the Huygens probe radio signal”. en. In: *Journal of Geophysical Research* 111.E7 (2006), E07001. ISSN: 0148-0227. DOI: 10.1029/2005JE002613.

[4] M.K. Bird et al. “Radio thermal emission from Pluto and Charon during the New Horizons encounter”. en. In: *Icarus* 322 (Apr. 2019), pp. 192–209. ISSN: 00191035. DOI: 10.1016/j.icarus.2019.01.004.

[5] T. Andert et al. “Bistatic Radar Observations of 67P/Churyumov-Gerasimenko”. In: *AGU Fall Meeting Abstracts*. Vol. 2017. Dec. 2017, P12A–01.

[6] A. Probst et al. “Mission concept selection for an asteroid mining mission”. en. In: *Aircraft Engineering and Aerospace Technology* 88.3 (May 2016), pp. 458–470. ISSN: 0002-2667. DOI: 10.1108/AEAT-11-2014-0199.

[7] “Planetary Exploration”. en. In: *Advances in Bistatic Radar*. Ed. by Nicholas J. Willis and Hugh D. Griffiths. Institution of Engineering and Technology, Jan. 2007, pp. 56–77. ISBN: 978-1-891121-48-7 978-1-61353-129-7. DOI: 10.1049/SBRA001E_ch5.

[8] T. Hagfors. “Backscattering from an undulating surface with applications to radar returns from the Moon”. In: \j*gr* 69 (Sept. 1964), pp. 3779–3784. DOI: 10.1029/JZ069i018p03779.

[9] Ahmed K. Sultan-Salem and G. Leonard Tyler. “Hagfors’ law revisited”. en. In: *Journal of Geophysical Research* 111.E6 (2006), E06S07. ISSN: 0148-0227. DOI: 10.1029/2005JE002489.

[10] R. A. Simpson. “Spacecraft studies of planetary surfaces using bistatic radar”. In: *IEEE Transactions on Geoscience and Remote Sensing* 31 (Mar. 1993), pp. 465–482. DOI: 10.1109/36.214923.

[11] H. Ling, R. -. Chou, and S. -. Lee. “Shooting and bouncing rays: calculating the RCS of an arbitrarily shaped cavity”. In: *IEEE Transactions on Antennas and Propagation* 37.2 (Feb. 1989),

pp. 194–205. ISSN: 1558-2221. DOI: 10.1109/8.18706.

[12] J. Baldauf et al. "High frequency scattering from trihedral corner reflectors and other benchmark targets: SBR versus experiment". In: *IEEE Transactions on Antennas and Propagation* 39.9 (Sept. 1991), pp. 1345–1351. ISSN: 1558-2221.

[13] Wei Gao, Binghuai Li, and Yiwen Tang. "A comparative study on the exit aperture in shooting and bouncing ray method". In: *2012 10th International Symposium on Antennas, Propagation and EM Theory, ISAPE 2012* (Oct. 2012), pp. 1248–1250. DOI: 10.1109/ISAPE.2012.6409006.

[14] Wei-Feng Huang et al. "GO/PO and PTD with Virtual Divergence Factor for Fast Analysis of Scattering from Concave Complex Targets". In: *IEEE Transactions on Antennas and Propagation* 63 (May 2015), pp. 1–1. DOI: 10.1109/TAP.2015.2405086.

[15] Y. Tao, H. Lin, and H. Bao. "GPU-Based Shooting and Bouncing Ray Method for Fast RCS Prediction". In: *IEEE Transactions on Antennas and Propagation* 58.2 (Feb. 2010), pp. 494–502. ISSN: 1558-2221. DOI: 10.1109/TAP.2009.2037694.

[16] Fatih Dikmen et al. "Implementation of an efficient shooting and bouncing rays scheme". In: 2010.

[17] Adrian Fung et al. "An Improved Iem Model for Bistatic Scattering From Rough Surfaces". In: *Journal of Electromagnetic Waves and Applications - J ELECTROMAGNET WAVE APPLICAT* 16 (Jan. 2002), pp. 689–702.

[18] Jonas Krumme. "Simulation of Radar for Planetary Surfaces on the GPU with RL-GO". MA thesis. Fachbereich 3, Universität Bremen, 2020.

[19] Matt Pharr, Wenzel Jakob, and Greg Humphreys. *Physically Based Rendering: From Theory to Implementation (3rd ed.)* 3rd. San Francisco, CA, USA: Morgan Kaufmann Publishers Inc., 2016, p. 1266. ISBN: 9780128006450.

[20] NVIDIA. *CUDA Toolkit Documentation - Thrust*. https://docs.nvidia.com/cuda/thrust/index.html. Accessed: 2020-09-23.

[21] F. Weinmann. "Ray tracing with PO/PTD for RCS modeling of large complex objects". In: *IEEE Transactions on Antennas and Propagation* 54.6 (June 2006), pp. 1797–1806. ISSN: 1558-2221. DOI: 10.1109/TAP.2006.875910.

[22] Prof. Sean Victor Hum. *Radio and Microwave Wireless Systems - Reflection/Refraction*. https://www.waves.utoronto.ca/prof/svhum/ece422/notes/17-reflrefr.pdf. Accessed: 2020-10-4.

[23] Jinzu Ji, Jun Liu, and Yunpeng Ma. "Triangular ray tubes in electromagnetic scattering calculation using shooting and bouncing ray (SBR)". In: *Optik* 127.5 (2016), pp. 3117–3120. ISSN: 0030-4026. DOI: https://doi.org/10.1016/j.ijleo.2015.12.080. URL: http://www.sciencedirect.com/science/article/pii/S0030402615019890.

[24] F. Preusker et al. *DAWN FC2 DERIVED VESTA DTM SPG V1.0, DAWN-A-FC2-5-VESTADTMSPG-V1.0*. 2016.

[25] Marc D. Rayman and Robert A. Mase. "Dawns exploration of Vesta". In: *Acta Astronautica* 94.1 (Jan. 2014), pp. 159–167. ISSN: 00945765. DOI: 10.1016/j.actaastro.2013.08.003.